REPORT

SOLAR PHYSICS

Decay of the coronal magnetic field can release sufficient energy to power a solar flare

Gregory D. Fleishman[1]*, Dale E. Gary[1], Bin Chen[1], Natsuha Kuroda[2,3], Sijie Yu[1], Gelu M. Nita[1]

Solar flares are powered by a rapid release of energy in the solar corona, thought to be produced by the decay of the coronal magnetic field strength. Direct quantitative measurements of the evolving magnetic field strength are required to test this. We report microwave observations of a solar flare, showing spatial and temporal changes in the coronal magnetic field. The field decays at a rate of ~5 Gauss per second for 2 minutes, as measured within a flare subvolume of ~10^{28} cubic centimeters. This fast rate of decay implies a sufficiently strong electric field to account for the particle acceleration that produces the microwave emission. The decrease in stored magnetic energy is enough to power the solar flare, including the associated eruption, particle acceleration, and plasma heating.

The solar corona sometimes exhibits an explosive release of the energy stored in magnetized plasma, which drives phenomena such as solar flares (*1*–*5*). The standard model of solar flares (*6*–*9*) posits that they are powered by magnetic energy stored in the solar corona and released (dissipated into other forms) through magnetic reconnection (*10*)—a reconfiguration of the magnetic field topology toward a state of lower magnetic energy. Changes in the coronal magnetic field during a flare or other large-scale eruption have been quantified only indirectly, for example (*11*), from extrapolations of the magnetic field measured at the photosphere—the surface layer of the Sun seen in white light. Although this method can quantify the modest magnetic energy transfer of ~10%, it is known to suffer from many shortcomings (*12*). The extrapolation approach does not allow the dynamic local changes of the magnetic field to be quantified at time scales short enough to characterize the flare energy release.

We report observations (*13*) of a large solar flare—one of several that occurred in September 2017. The partially occulted eruptive flare occurred in active region (AR) 12673, at heliographic coordinates 9° south, 91° west (Fig. 1A), on 10 September 2017. This event exhibits the main ingredients of the standard flare model, including a cusplike structure of nested magnetic loops that evolves upward at a speed of ~30 km s^{-1} and an apparent current sheet (Fig. 1A) (*14*–*16*). This eruptive flare was widely observed at many wavelengths (*14*–*19*). Estimates of the kinetic, thermal, and nonthermal energies released in the flare are available from complementary approaches and datasets, whereas the dominant magnetic energy has only been estimated indirectly (*20*). Figure 1 shows context information for the flare, including the microwave images that we observed using the Expanded Owens Valley Solar Array (EOVSA) (*21*) in 26 microwave bands in the range of 3.4 to 15.9 GHz (*13*).

We produced magnetic field maps from these observations (*13*), examples of which are shown in Fig. 2. The full sequence is shown in movie S1. They show strong variation between maps, demonstrating the fast evolution of the coronal magnetic field strength B. The magnetic field strength decays quickly at the cusp region; away from that region, the field also decays but more slowly.

To quantify this decay, Fig. 3 shows the time evolution of the flaring coronal magnetic field at two locations marked in Fig. 2. Both locations exhibit a decay in the magnetic field strength but with different timing. One location shows a decay of the magnetic field from ~600 to ~200 G over ~1 min, a magnetic field decay rate of $|\dot{B}| \approx 6.6\ \mathrm{G\ s^{-1}}$. The decay ends at about 15:58 Coordinated Universal Time (UTC), after which the magnetic field at this location remains roughly constant. By contrast, the location within a larger and higher collapsing loop, marked in Fig. 1A, experiences a longer decay, until roughly 16:00 UTC. In this location, the magnetic field decays from ~900 to ~250 G over ~2 min, a rate of $|\dot{B}| \approx 5.4\ \mathrm{G\ s^{-1}}$. The energy release suggested by this magnetic

[1]Center for Solar Terrestrial Research, New Jersey Institute of Technology, University Heights, Newark, NJ 07102, USA. [2]University Corporation for Atmospheric Research, Boulder, CO 80307, USA. [3]Space Science Division, Code 7684, Naval Research Laboratory, Washington, DC 20375, USA.
*Corresponding author. Email: gfleishm@njit.edu

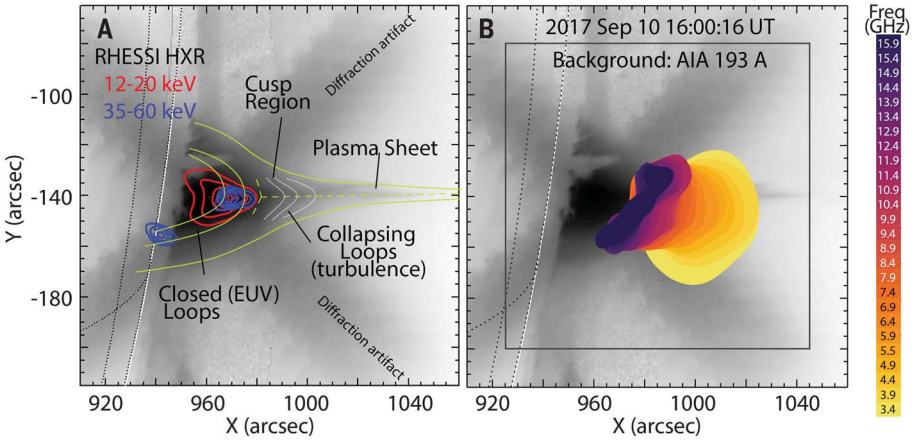

Fig. 1. Multiwavelength observations of the class X8 flare on 10 September 2017. (**A**) An EUV image (193 Å) with inverted brightness overlain with contours outlining the thermal (red contours) and nonthermal (blue contours) hard x-ray (HXR) emission (*16*). The green and white lines are a schematic drawing of the plasma sheet (the current sheet, according to the standard solar flare model), closed and collapsing (newly reconnected) loops, and the cusp region, where the fastest evolution of the magnetic field takes place. Only one of the loop foot points (the southern one) is located on the visible side of the disk, whereas the other is located behind the limb (occulted by the Sun). The thin white curve shows the solar surface (photosphere). The dotted black lines indicate the solar coordinate grid marked at 5° intervals. X and Y are the Cartesian coordinates with the coordinate center adopted in the center of the solar disk. RHESSI, Reuven Ramaty High Energy Solar Spectroscopic Imager. (**B**) The same image as (A), overlain with the microwave observations taken with EOVSA. The colored regions indicate the ≥50% brightness areas corresponding to 26 frequencies from 3.4 to 15.9 GHz. The relationships among different data sources suggest that the microwave emission comes from the cusp region, outlining the newly reconnected collapsing field lines. The gray box outlines the region of corresponding magnetic field maps in Fig. 2. AIA, Atmospheric Imaging Assembly; Freq., frequency.

field decay ends around the time of the peak microwave emission (16:00 UTC), which is consistent with the theoretical predictions of microwave emission arising from a population of trapped electrons (*16*).

We compare these measurements of the decaying coronal magnetic field with equilibrium models that are based on extrapolation of photospheric magnetic field measurements (*11*). The extrapolation requires corresponding photospheric vector magnetic field data, which are not available for this partially occulted event. However, magnetic field models are available (*22*) for this AR a few days earlier, on 6 September 2017, when this AR could be seen more face-on. These models found that the strongest magnetic field in the corona at the height of 30 Mm was ~200 G [figure 5 in (*22*)]. Our measurements at that height match this model value at the end of the time range analyzed, after the decay of the magnetic field is over, which implies that the magnetic field in the flare evolves toward an equilibrium state. However, the much stronger values observed earlier in the flare are several times as high as the equilibrium values. This indicates that a dynamic, transient magnetic field was lifted up from lower heights by the eruption process. This redistribution of the strong magnetic field—originally located low in the corona—over a much larger coronal volume during the flare might power the solar flare and associated eruption.

The Faraday equation is $\dot{\mathbf{B}} = -c\nabla \times \mathbf{E}$ (where **B** and **E** are the magnetic and electric field vectors, respectively, and c is the speed of light), which requires that an electric field be associated with the observed decay in magnetic field strength. Estimating $|\nabla \times \mathbf{E}|$ as E/R, where R is the scale of nonuniformity at the cusp region, and adopting representative values $\dot{B} \approx 5\,\mathrm{G\,s^{-1}}$ and $R \approx 3.65 \times 10^8$ cm—equivalent to 5 arc sec on the Sun, which is the size of the smallest coherent structures in the magnetic maps [as well as in extreme ultraviolet (EUV) images (*15*)]—we find $E \sim 20\,\mathrm{V\,cm^{-1}}$. For comparison, the Dreicer field, which demarcates regimes of the steady electric current and free runaway of the plasma electrons (*23*), is $E_D \sim 10^{-4}\,\mathrm{V\,cm^{-1}}$. This field strength E is consistent, within an order of magnitude, with available indirect estimates (*10*, *24*, *25*) for other large flares. Our choice of the scale $R \approx 5$ arc sec is ~10 to 20% of the cusp size and represents the macroscopic structure. It does not preclude the existence of smaller-scale structures and the proportionally smaller electric fields associated with them. However, the derived electric field remains above the Dreicer value for any scales $\gtrsim 5 \times 10^{-5}$ arc sec.

The decrease in magnetic energy at the cusp region must be associated with a conversion of that energy into other forms. An energy source is needed at the cusp region of this event to account for its enhanced temperature (*15*). The magnetic-field–aligned component of our inferred electric field should accelerate particles as required to power the microwave emission and could drive the observed enhanced heating at the cusp region (*15*).

The decay in magnetic field strength implies advection and/or diffusion of the magnetic field, which can be estimated using the induction equation, $\dot{\mathbf{B}} = \nabla \times [v \times \mathbf{B}] + \nu\nabla^2\mathbf{B}$, where v is the plasma velocity and ν is the magnetic diffusivity. The advection term, $\nabla \times [v \times \mathbf{B}]$, can easily account for the magnetic field variation during the phase of apparent upward motion of the arclike structures in the magnetic field maps from 15:57:00 to 15:59:25 UTC (movie S1). However, at later times these arclike structures fade without moving, which implies dissipation of the magnetic field, not advection. We estimate the magnetic diffusivity ν required to drive the apparent decay rate ($|\dot{B}| \approx 5\,\mathrm{G\,s^{-1}}$) of the magnetic field ($B \approx 600$ G) as $\nu \sim R^2\,\dot{B}/B \sim 10^{15}\,\mathrm{cm^2\,s^{-1}}$. This value of ν is much larger than the magnetic diffusivity due to Coulomb collisions (*26*). It can only be provided by turbulent magnetic diffusion, which appears when a large fraction of the velocity v entering the induction equation is fluctuating [turbulent-like (*27*)], rather than steady. Averaging the induction equation over the random velocity field results in a renormalization of the magnetic diffusivity coefficient (*26*) such that $\nu \sim u\,R/3$, where u is the typical turbulent velocity. Nonthermal turbulent velocities of $u \sim 100\,\mathrm{km\,s^{-1}}$ were measured at the cusp region in this flare (*15*), which implies $\nu \sim u\,R/3 \sim 1.2 \times 10^{15}\,\mathrm{cm^2\,s^{-1}}$, in agreement with the estimate obtained from $\dot{B}$ above.

Figure 3B shows the evolution of the mean magnetic energy density (*13*) in this region. Over ~1.5 min, the magnetic energy density decays at a rate of ~200 erg $\mathrm{cm^{-3}\,s^{-1}}$, losing ~80% of the magnetic energy available in this area. The net decrease of the magnetic energy in the adopted nominal flare volume of $10^{28}\,\mathrm{cm^3}$, which corresponds to a source with a linear scale of ~20 Mm (Fig. 1), is $\sim 2 \times 10^{32}$ erg.

We compare this reduction in magnetic energy density with the energy density of nonthermal electrons (microwave diagnostics provides the instantaneous electron and energy densities, unlike x-ray diagnostics, which provides electron and energy flux), which we compute from the same data (*13*). Figure 3B

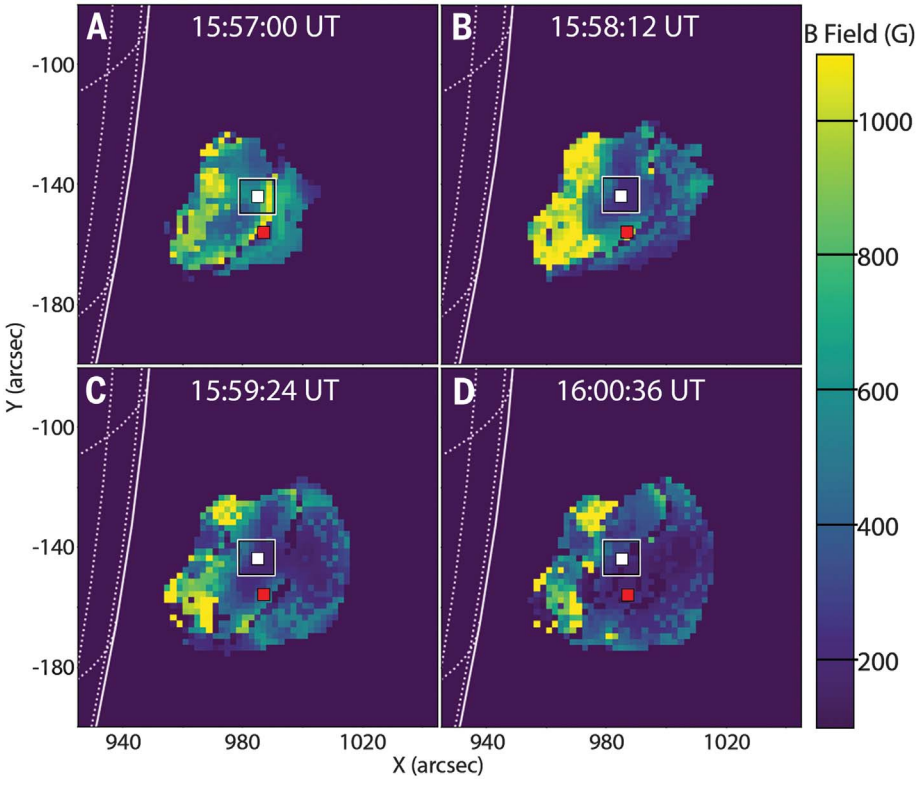

Fig. 2. Evolving maps of the coronal magnetic field. (**A** to **D**) Four coronal magnetic field maps derived for the 10 September 2017 flare, separated by 72 s. Apparent upward motion of the radio source and looplike structures in the magnetic field maps is visible in panels (A) to (C), showing the spreading of the reconnection process upward. Red and white squares, and the empty white box, correspond to locations shown in Fig. 3. The solar coordinate grid and the solar photosphere are shown by the white dotted and solid lines, respectively. Movie S1 shows an animated version of this figure.

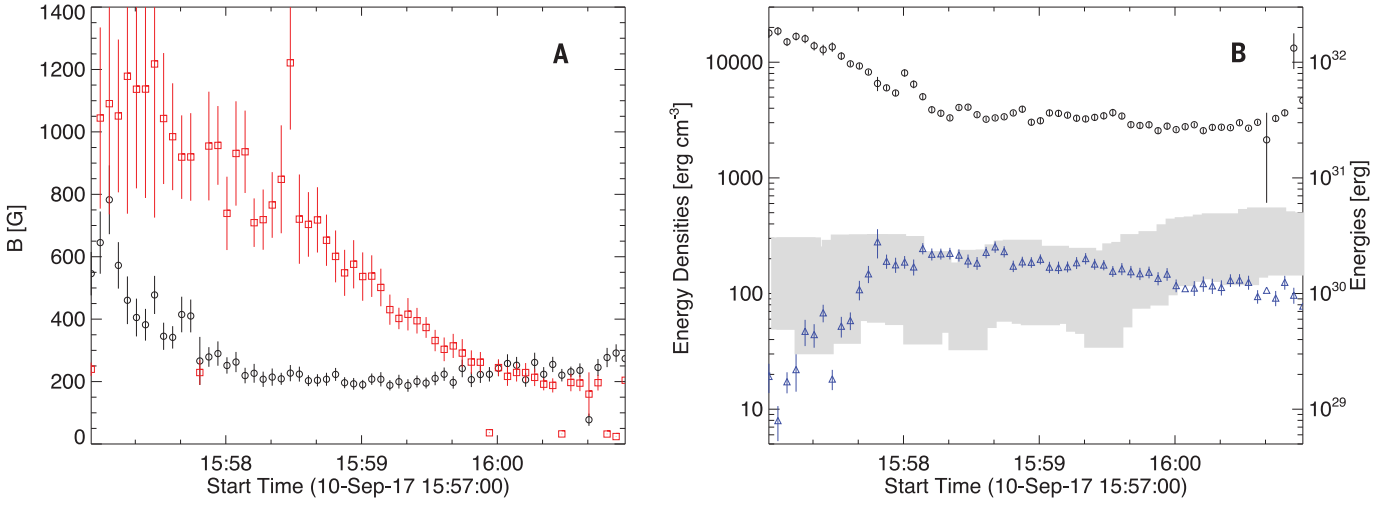

Fig. 3. Evolution of the magnetic field and magnetic energy. (**A**) Evolution of the magnetic field at two locations shown in Fig. 2. The red and black symbols show the data from the red and white squares, respectively. Black circles show decay of the magnetic field from 15:57 to 15:58 UTC, remaining roughly constant after that. The red squares, which correspond to a higher member of the system of nested loops, show a similar decay lasting 2 min longer, coinciding with the apparent upward motion of the EUV loops (Fig. 2). Error bars show 1σ uncertainties. (**B**) The mean magnetic energy density w_B (black circles) and the mean energy density of nonthermal electrons w_{nth} (blue triangles), both computed within the white box shown in Fig. 2. The shaded gray area indicates our estimated range of thermal energy density computed in (*13*). The right axis shows the corresponding total energy, assuming a flare volume of 10^{28} cm^3. Error bars show 1σ uncertainties.

shows the evolution of the (lower bound of the) nonthermal energy density, assuming a power-law distribution of electrons with a low-energy cutoff of E_{min} = 20 keV (*13*). Although this nonthermal energy constitutes only a few percent of the decrease in magnetic energy, it appears that the main decay of the magnetic energy is correlated in time with the increase of the nonthermal electron energy. This result implies that a direct energy conversion occurs in this region. The thermal energy density and kinetic energy density of turbulent motions cannot be estimated from the microwave diagnostics alone but require additional inputs based on available EUV diagnostics (*15*). The estimated thermal energy density (*13*) is also shown in Fig. 3B. It overlaps with the lower bound of the nonthermal energy density obtained above. The kinetic energy associated with random motions of the plasma is two orders of magnitude lower than the thermal energy. This implies that we observe a region at the cusp location—where available magnetic energy is converted to other forms of flare energy—which occurs below, but not within, the reconnection current sheet. The observed release of the magnetic energy is sufficient to power all other observed forms of energy in the flare.

Our observations quantify the coronal magnetic energy at the flare site and establish exactly where and how fast it is released. Our findings provide a quantitative observation of energy transformation in a solar flare, linking the thermal and nonthermal energy components to the associated magnetic energy release.

REFERENCES AND NOTES

1. T. Yokoyama, K. Shibata, *Nature* **375**, 42–44 (1995).
2. B. Kliem, T. Török, *Phys. Rev. Lett.* **96**, 255002 (2006).
3. K. Shibata *et al.*, *Science* **318**, 1591–1594 (2007).
4. S. Scaringi, T. J. Maccarone, C. D'Angelo, C. Knigge, P. J. Groot, *Nature* **552**, 210–213 (2017).
5. P. F. Wyper, S. K. Antiochos, C. R. DeVore, *Nature* **544**, 452–455 (2017).
6. H. Carmichael, in *The Physics of Solar Flares, Proceedings of the AAS-NASA Symposium held 28-30 October, 1963 at the Goddard Space Flight Center, Greenbelt, MD*, W. N. Hess, Ed. (National Aeronautics and Space Administration, 1964), vol. 50, p. 451.
7. P. A. Sturrock, *Nature* **211**, 695–697 (1966).
8. T. Hirayama, *Sol. Phys.* **34**, 323–338 (1974).
9. R. A. Kopp, G. W. Pneuman, *Sol. Phys.* **50**, 85 (1976).
10. E. Priest, T. Forbes, *Magnetic Reconnection* (Cambridge Univ. Press, 2007).
11. X. Sun *et al.*, *Astrophys. J.* **748**, 77 (2012).
12. M. L. DeRosa *et al.*, *Astrophys. J.* **696**, 1780–1791 (2009).
13. Materials and methods are available as supplementary materials.
14. Y. Li *et al.*, *Astrophys. J.* **853**, L15 (2018).
15. H. P. Warren *et al.*, *Astrophys. J.* **854**, 122 (2018).
16. D. E. Gary *et al.*, *Astrophys. J.* **863**, 83 (2018).
17. N. Omodei, M. Pesce-Rollins, F. Longo, A. Allafort, S. Krucker, *Astrophys. J.* **865**, L7 (2018).
18. D. M. Long *et al.*, *Astrophys. J.* **855**, 74 (2018).
19. G. A. Doschek *et al.*, *Astrophys. J.* **853**, 178 (2018).
20. D. Longcope, J. Unverferth, C. Klein, M. McCarthy, E. Priest, *Astrophys. J.* **868**, 148 (2018).
21. G. M. Nita, J. Hickish, D. MacMahon, D. E. Gary, *J. Astron. Instrum.* **05**, 1641009 (2016).
22. S. A. Anfinogentov, A. G. Stupishin, I. I. Mysh'yakov, G. D. Fleishman, *Astrophys. J.* **880**, L29 (2019).
23. H. Dreicer, *Phys. Rev.* **115**, 238–249 (1959).
24. J. Qiu, D. E. Gary, G. D. Fleishman, *Sol. Phys.* **255**, 107–118 (2009).
25. G. D. Fleishman *et al.*, *Astrophys. J.* **822**, 71 (2016).
26. G. D. Fleishman, I. N. Toptygin, *Cosmic Electrodynamics: Electrodynamics and Magnetic Hydrodynamics of Cosmic Plasmas* (Springer 2013).
27. J. T. Dahlin, J. F. Drake, M. Swisdak, *Phys. Plasmas* **24**, 092110 (2017).

ACKNOWLEDGMENTS

We thank the scientists and engineers who helped design and build EOVSA, especially G. Hurford, S. White, J. McTiernan, W. Grammer, and K. Nelin. **Funding:** This work was supported in part by NSF grants AGS-1817277, AST-1910354, and AGS-1654382 and NASA grants NNX17AB82G, 80NSSC18K0667, 80NSSC19K0068, and 80NSSC18K1128 to the New Jersey Institute of Technology. N.K. was partially supported by the NASA Living With a Star Jack Eddy Postdoctoral Fellowship Program, administered by UCAR's Cooperative Programs for the Advancement of Earth System Science (CPAESS). **Author contributions:** G.D.F. developed the methodology, performed the model fitting, analyzed the results, and wrote the draft manuscript; D.E.G. led the construction and commissioning of the EOVSA and developed the observational strategy and calibration for microwave spectroscopy; B.C. developed the microwave spectral imaging and self-calibration strategy; N.K. wrote software used in the analysis and visualization; D.E.G., B.C., and S.Y. prepared the microwave observation data; S.Y. implemented the microwave imaging pipeline under the guidance of D.E.G. and B.C.; and G.M.N. developed software used in modeling and testing the spectral fitting methodology and developed the GSFIT spectral fitting package. All authors discussed the interpretation of the data, contributed scientific results, and helped prepare the paper. **Competing interests:** The authors declare no competing interests. **Data and materials availability:** Raw EOVSA observational data used for this study are available at www.ovsa.njit.edu/fits/IDB/20170910/IDB20170910155625/. Fully processed EOVSA spectral imaging data (in IDL save format) are available at http://ovsa.njit.edu/publications/fleishman_ea_science_2019/data/. The microwave data fitting software, GSFIT, is available in the community-contributed SolarSoftWare repository, under the packages category, at www.lmsal.com/solarsoft/ssw/packages/gsfit/.

SUPPLEMENTARY MATERIALS

science.sciencemag.org/content/367/6475/278/suppl/DC1
Materials and Methods
Figs. S1 and S2
References (*28*–*33*)
Movies S1 and S2

13 April 2019; accepted 4 December 2019
10.1126/science.aax6874

Decay of the coronal magnetic field can release sufficient energy to power a solar flare

Gregory D. Fleishman, Dale E. Gary, Bin Chen, Natsuha Kuroda, Sijie Yu and Gelu M. Nita

Science **367** (6475), 278-280.
DOI: 10.1126/science.aax6874

Magnetic energy release in a solar flare

Solar flares are bright flashes and associated eruptions of plasma from the Sun that are thought to be powered by violent rearrangement of the magnetic fields near sunspots. Fleishman *et al.* observed a bright solar flare with a microwave interferometer, allowing them to map the magnetic field in the solar corona and monitor how it changed during the flare. They found a large drop in the local field strength over 2 minutes, releasing enough magnetic energy to power the entire solar flare. Determining the origin of this energy will help to predict how strong future solar flares may be and their potential space weather impacts on Earth.

Science, this issue p. 278

Supplementary Materials for

Decay of the coronal magnetic field can release sufficient energy to power a solar flare

Gregory D. Fleishman*, Dale E. Gary, Bin Chen, Natsuha Kuroda, Sijie Yu, Gelu M. Nita

*Corresponding author. Email: gfleishm@njit.edu

Published 17 January 2020, *Science* **367**, 278 (2020)
DOI: 10.1126/science.aax6874

This PDF file includes:

Other Supplementary Material for this manuscript includes the following:
(available at science.sciencemag.org/content/367/6475/278/suppl/DC1)

Movies S1 and S2 (.mp4)

Materials and Methods

Overview

We used data from the Expanded Owens Valley Solar Array (*21*) (EOVSA), which provided microwave images of the solar flare at hundreds of frequencies, combined into 30 spectral windows (*16*). EOVSA provides microwave images of the entire Sun with a time cadence of 1 s with high spatial (a few arcsec) and spectral (a few MHz) resolutions over the frequency range 1-18 GHz. This combination of high cadence and high spatial and spectral resolutions enables (*28, 29*) dynamical measurement of the evolving coronal magnetic field along with other rapidly changing physical parameters of solar flares. The microwave spectra have sufficient spatial resolution to investigate an almost uniform fraction of the (generally highly inhomogeneous) flaring region. The spectra from such (quasi-)uniform sub-volumes are fitted with a uniform-source model, which includes the gyrosynchrotron and free-free emission processes (see below). Sequential model fitting of the spectra from each pixel with sufficient microwave emission in each time range yields evolving parameter maps, which we computed with a cadence of one map every four seconds. We employed the evolving magnetic maps to study the spatially resolved structure and evolution of the magnetic field strength and the magnetic energy.

Description of the EOVSA Instrument and Data

EOVSA (*16, 21*) is a solar-dedicated radio array located at Owens Valley, California, USA. The array consists of thirteen 2-m antennas which at the time of these observations observed the Sun over the 2.5–18 GHz frequency range, covering that range every 1 s. The array also includes a 27-m antenna used for calibration on cosmic sources. The 13 small antennas form an interferometer with 78 baselines. For the event described in this Report we used imaging data above 3.4 GHz (*16*) split over 26 spectral windows (spws) of width 160 MHz with equally spaced central frequencies $f = 2.92 + n/2\,\mathrm{GHz}$, where n is the number of the spw from 1 to 26.

A detailed description of the imaging for the 2017 September 10 event is given in an earlier paper, (*16*). The nominal full-width-half-max (FWHM) spatial resolution of these observations is elliptical, with major axis $113.''7/f$[GHz] and minor axis $53.''0/f$[GHz]. The microwave image deconvolution procedure used the standard CLEAN algorithm (*30*). A circular restoring beam was used of FWHM $87.''9/f$[GHz] for frequencies up to 14.9 GHz, while the size was fixed at $6''$ above 15 GHz. Thus, the frequency range of 3.4–18 GHz corresponds to a restored range of $25.''7$–$6.''0$. However, for convenience in spectral fitting (see below), the cell size used in creating the images was fixed at $2'' \times 2''$ at all frequencies, which provides three samples across a resolution element at the highest frequencies (>15 GHz), and increasingly oversamples at lower frequencies.

The microwave multi-frequency images from EOVSA are combined by fitting models to the spatially resolved spectra sequentially, pixel-by-pixel and time-frame-by-time-frame, with a uniform-source function.

Microwave Spectral Fitting Technique

The microwave imaging spectroscopy data can be considered as a four-dimensional (4D) data cube with two spatial dimensions (x and y in the images), one temporal dimension (time), and one spectral dimension (frequency). We adopt the microwave Spectral Fitting Technique (*28, 29*), which attempts to fit a model to each spectral instance—the spectrum from a given pixel obtained at a given time—using a physically motivated model ("cost" function), based on the assumption of a homogeneous source. This can only be applied to a sufficiently small portion of the source that it can plausibly be approximated by a (quasi-)uniform source in the xy plane. We ignore the unavoidable line-of-sight (LOS) ambiguity along the z coordinate except in cases where it produces multiple spectral peaks; see below. The robustness of the homogeneous source assumption has been investigated using simulations (*29*).

Microwave continuum bursts in solar flares are typically produced by nonthermal electrons spiralling in the ambient magnetic field with, perhaps, some contribution of free-free emission (*31*) from the ambient thermal plasma, so the cost function must include a combination of the gyrosynchrotron (GS) and free-free processes. The source function describing free-free emission is relatively simple (*26*), while that for the GS process is more complicated and its exact numerical implementation is computationally expensive. We use Fast Gyrosynchrotron Codes (*32*), which reduce the time needed to compute a GS spectrum. These codes were used to compute the cost function in the practical forward model fitting (*28, 29*) codes we employed. Specifically, the cost function represents a solution of the radiation transfer equation that includes GS and free-free emissivity and absorption in a uniform source having a projected area of $2'' \times 2''$, depth $d = 5.8\,$Mm along the line-of-sight (equivalent to $8''$ if viewed in the sky plane, taken to be roughly equal to the width of flaring loops), and a number (typically, six) of free parameters to be determined from the model fitting. A typical set of free parameters is: the magnitude of the magnetic field B (which we allow to vary in the range 1 G to 3000 G), the angle θ between the magnetic field vector and the line-of-sight (from 20° to 90°), the thermal plasma density n_{th} (from 10^8 to 6×10^{11} cm^{-3}), the nonthermal electron density n_{nth} (from 10^3 to 2×10^{10} cm^{-3}) above a preset low-energy cutoff $E_{\rm min}$ (assumed to be $E_{\rm min} = 20$ keV), the spectral index δ (from 1.1 to 15), and the high-energy cutoff $E_{\rm max}$ (from 0.1 to 10 MeV). The latter three parameters plus $E_{\rm min}$ are used to determine the total energy in nonthermal particles, shown in Fig. 3. The forward model fitting employs the SIMPLEX minimization scheme (*33*) to find a local minimum of the given functional in a multi-dimensional parameter space, complemented by "shaking" that strongly perturbs the solution obtained by SIMPLEX, to overcome any local minimum to locate (as close as possible) the global minimum. The model fitting code also returns the uncertainty of each fit parameter computed as the range of this parameter variation within which the solution remains within the confidence interval (of one sigma), inde-

pendent of other parameter variations. The actual scatter of the derived parameters is consistent with these error bars; see Fig. 3A.

Tests (*28, 29*) with simulated microwave data based on 3D flare models have established that the algorithm recovers the source parameters in most cases; especially when the spectral peak lies within the spectral range of the instrument and the low- and high-frequency slopes are well constrained. The high-frequency (optically thin) slope of the microwave spectrum constrains the slope in the energy spectrum of nonthermal electrons and the low-frequency (optically thick) spectral range constrains the effective energy of radiating electrons. This effective energy depends mainly on the spectral index (fixed by the high-frequency slope) and the magnetic field strength. The peak frequency depends on the magnetic field and the number density of the nonthermal electrons, while the shapes of low- and high- frequency spectral regions depends, respectively, on the thermal plasma density (via Razin-effect (*32*) and/or free-free contribution) and the high-energy cutoff (which is, however, rather poorly constrained in most of the cases studied here); Movie S2 shows these trends, where for clarity we only vary each parameter by a factor of two. In the real fitting process the parameters can vary within much broader limits; see above.

EOVSA can provide spatially resolved spectra similar to the simulated data (*28, 29*) and, thus, our data are appropriate for performing dynamic coronal magnetography of flaring regions. As discussed above, the spatial resolution of the images is frequency dependent, while for the fitting we employ the frequency-independent pixel size of $2'' \times 2''$, which is similar to the spatial resolution at the highest frequencies. This implies that the lower-frequency emission from such a pixel effectively involves some averaging due to leakage from the surrounding pixels pertaining to the same resolution element at a given frequency. This issue was investigated using simulated data (*29*). Specifically, a solution that makes up for the potential negative effect of this averaging is adding an additional, frequency-dependent error to the formal rms

errors, to apportion a progressively smaller weights to the lower-frequency data points during our model fitting. It was found (*29*) that such an approach works except at the source edges, where the effect of the frequency-dependent spatial resolution yields apparent fitting artifacts. An alternative to this approach could be the use of a larger pixel for the fitting corresponding to the resolution element at a low frequency. In the simulations reported by (*29*), however, it was found that in most cases this would result in deviations from a uniform source spectrum, thus, invalidating the technique. Therefore, we proceed with the smallest possible pixel size and frequency-dependent weights (*29*).

However, the real data offer a wider variety of cases than found in simulations (*29*). Figure S1 shows a set of spectra obtained from various pixels during the main phase of the 2017 September 10 flare. Figure S1A shows two examples of single-component spectrum (i.e., a spectrum having a single peak) and their fits by the adopted uniform source model. Although one of them has a second component rising at high frequencies, the high-frequency data points have relatively large uncertainties in this instance and, thus, small fitting weights. As a result, the automated fit effectively ignores the high-frequency component, while closely fits the low-frequency component. All quantitative results presented in the Report are based on similarly good spectra and reliable fits.

Figure S1B-C display more problematic cases, which we did not use for quantitative analysis. Figure S1B shows two cases of spectra that do not contain a peak, but continue rising at the highest observed frequencies. Diagnostics based on such cases are possible, but have higher uncertainty. Figure S1C presents two cases when the presence of two spectral components affects the model fitting. Although in principle such cases might be used quantitatively, they would require a modification of the cost function to include two sources along LOS, so we discard them.

As an example, all 60 spectra covering 60 sequential time frames from the white square in

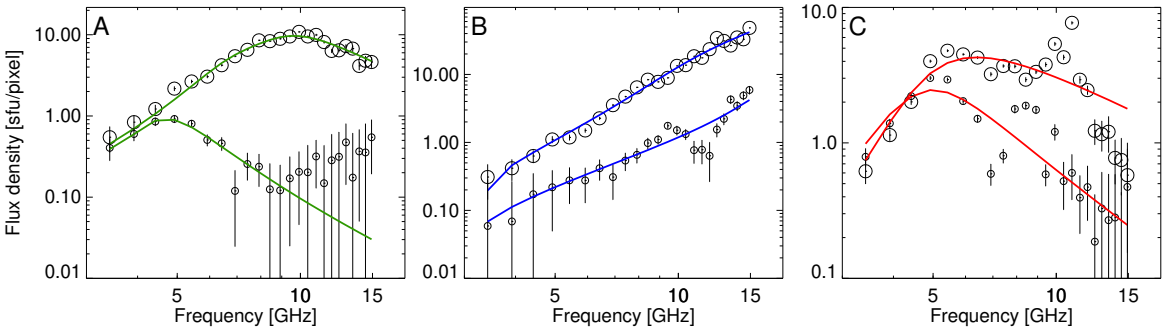

Fig. S1: **Example spectra and models fitted to them.** A: Two examples of single-component spectra having the spectral peak within the observed frequency range, which are both well-suited for our spectral model fitting. Although the spectrum shown by small circles does show a second component (perhaps a result of an imaging sidelobe) at high frequencies, it has large uncertainties so receives a low weight in the fitting process, which retrieves the main, low-frequency spectral peak. Error bars show the statistical uncertainties, obtained by selecting an area away from the source and computing the root-mean-square (rms) of the background fluctuations. B: Two examples of single-component spectra, where the spectral peak falls outside the observed range of frequencies. Model fitting of these spectra is statistically justified, but might not be unique. C: Two examples of two-component spectra, which cannot be adequately fitted using a single-component source model. All quantitative results in this Report are based solely on well-constrained models similar to those shown in panel A. The fluxes are given in Solar Flux Units (sfu): 1 sfu = 10^4 Jy = 10^{-22} Wm^{-2}Hz^{-1} = 10^{-19} erg s^{-1}cm^{-2}Hz^{-1}.

Fig. 2 are shown in Fig. S2. All these spectra are similar to those in Fig. S1A, and all but one of the model fits closely match the data points.

The derived evolution of the magnetic field can, in principle, be used to quantify the magnetic energy, energy density, and their evolution at the flaring volume. However, as we have shown above, not all elementary spectra are reliably fitted by our automated fitting procedure. Thus, it might not be reliable to integrate over the entire flaring region. We inspected our magnetic field maps and identified an area, marked by a white box in Fig. 2, where most of the spectra are smooth and single-component like those in Fig. S1A, and therefore the vast majority of the fits are reliable (see Fig. S2).

A Consistency Check

To check the numbers of the magnetic field, its derivative, and the associated electric field for consistency, we exploit previous observations that the microwave source moves upward with velocity $v \approx 30$ km s^{-1} (*16*), likely tracing the process of upward spreading of the magnetic reconnection. This velocity, because of magnetic connectivity with the photosphere, should have an associated ribbon-spreading velocity commonly used to estimate the reconnection electric field (*24*). Hence, the reconnection electric field can be estimated as E [V cm^{-1}] $\approx 10^{-3}B[\mathrm{G}]v[\mathrm{km/s}]$. Taking the above estimate of the electric field (20 V cm^{-1}) and velocity $v \approx 30$ km s^{-1}, we obtain an estimate of $B \sim 600$ G, which is within the range of the varying magnetic field in Fig. 3A. This confirms that our measured values of the magnetic field and its derivative are mutually consistent.

Magnetic, Nonthermal, Thermal, and Kinetic Energies

The magnetic and nonthermal energy densities are constrained by the model fitting parameters. The magnetic energy density $w_B = B^2/8\pi$ is determined by the magnetic field strength at each location and time frame. We compute the mean energy density of the magnetic field by averaging over all locations in the white box shown in Fig. 2. The total magnetic energy of the flare is a product of the energy density and the flare volume.

The energy density of nonthermal electron component $w_{nth} = \frac{\delta-1}{\delta-2}E_{\min}n_{nth}$ is computed above the cutoff energy $E_{\min}$ at each location and time frame. The mean nonthermal energy density is computed by averaging over all locations in the white box shown in Fig. 2. The total nonthermal energy of the flare is a product of the energy density and the flare volume. The uncertainties of the magnetic and nonthermal energy (density) are computed by propagation of errors of the model fitting parameters used to compute these energy densities.

To estimate the mean thermal energy density over the same area as in case of magnetic and

nonthermal energies, we employed the thermal densities obtained from our model fitting. The temperature, however, is not constrained by the model. EUV data have allowed the temperature to be estimated as $T \approx 20$ MK (*15*) but for different locations and time frames. Given that we do not know exact values of the temperature for our time frames and individual pixels, we adopt a likely range of the flare plasma temperatures 10–30 MK. The thermal energy density is $w_T \approx 3k_B n_{th} T$ erg cm^{-3}, where k_B is the Boltzman constant, then the thermal energy is a product of the energy density and the volume.

Similarly, the kinetic energy density is $\rho u^2/2$, where $\rho \approx n_e m_p$ is the plasma mass density, m_p is the proton mass, u is the turbulent velocity. The nonthermal turbulent velocity were measured from EUV spectral data (*15*) as $u \sim 100$ km s^{-1}. Then, the kinetic energy is the product of the kinetic energy density and the volume.

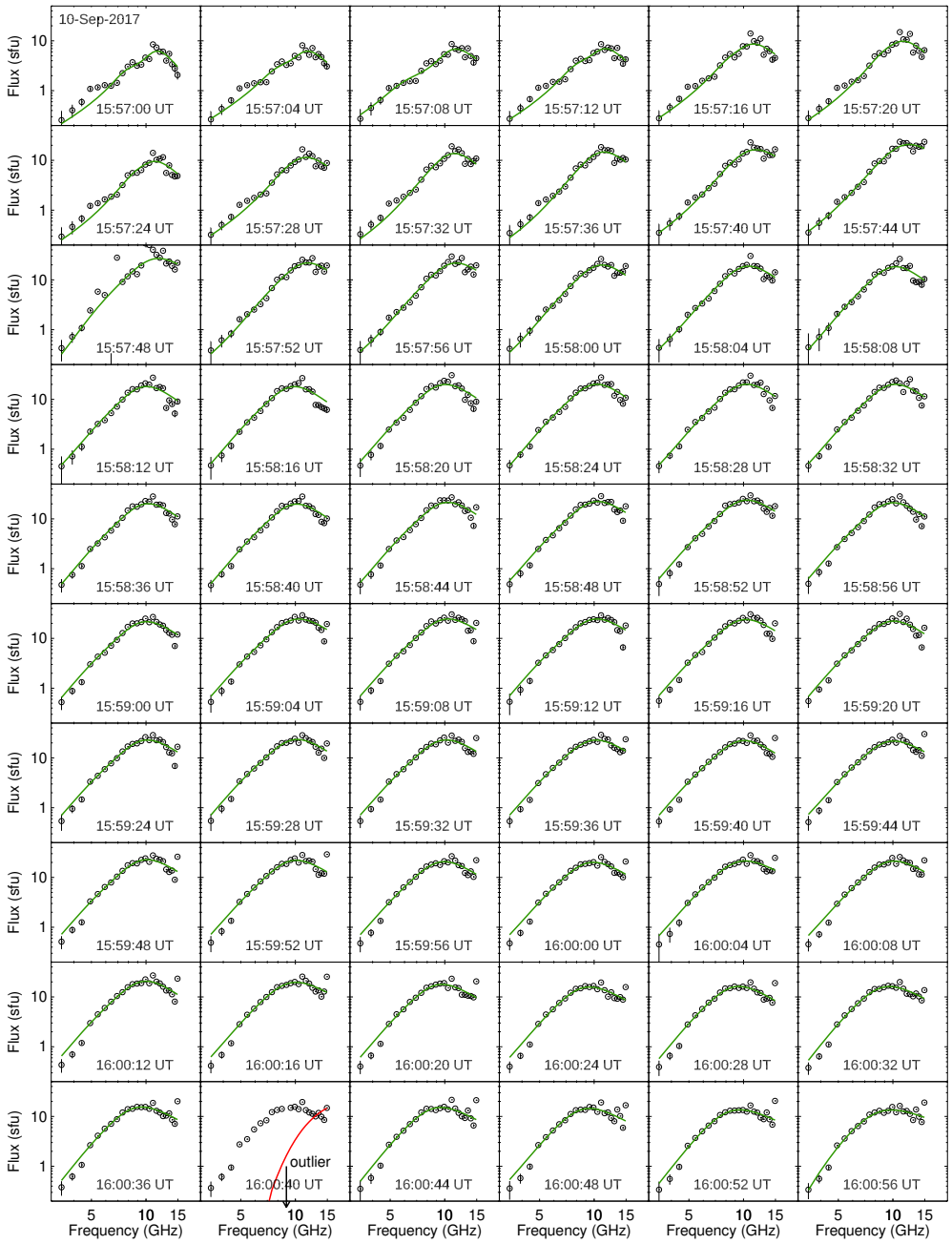

Fig. S2: **Spectra and fitted models for all time frames for a single pixel.** Sixty consecutive spectra and fits from the location marked with the white square in Fig. 2 are shown, along with the models fitted to them. During its evolution, the spatially resolved spectrum remains single-component, and all but one of the fits closely match the data points. A poor fit is shown in red (bottom row), which we ascribe to an artifact of a glitch in the data—an anomalously low flux level at one of the frequencies on 16:00:40 UT indicated by the downward pointed arrow.

Captions for Movies

Movie S1. Evolving maps of the coronal magnetic field. This movie demonstrates evolution of the coronal magnetic field in the 2017 September flare over the four minutes. Each frame is separated by 4 seconds. Solid white curve outlines the edge of the solar surface. The dotted curves show the solar coordinate grid.

Movie S2. Sensitivity of microwave spectra to variation of source parameters. This movie demonstrates how the two polarized components (ordinary mode; dashed line; and extraordinary mode; solid line) of the microwave emission vary when the parameters of the emission source change one by one. The total microwave intensity, used in this study, is the sum of these two polarized components.

References and Notes

1. T. Yokoyama, K. Shibata, Magnetic reconnection as the origin of X-ray jets and Hα surges on the Sun. *Nature* **375**, 42–44 (1995). doi:10.1038/375042a0

2. B. Kliem, T. Török, Torus instability. *Phys. Rev. Lett.* **96**, 255002 (2006). doi:10.1103/PhysRevLett.96.255002 Medline

3. K. Shibata, T. Nakamura, T. Matsumoto, K. Otsuji, T. J. Okamoto, N. Nishizuka, T. Kawate, H. Watanabe, S. Nagata, S. Ueno, R. Kitai, S. Nozawa, S. Tsuneta, Y. Suematsu, K. Ichimoto, T. Shimizu, Y. Katsukawa, T. D. Tarbell, T. E. Berger, B. W. Lites, R. A. Shine, A. M. Title, Chromospheric anemone jets as evidence of ubiquitous reconnection. *Science* **318**, 1591–1594 (2007). doi:10.1126/science.1146708 Medline

4. S. Scaringi, T. J. Maccarone, C. D'Angelo, C. Knigge, P. J. Groot, Magnetically gated accretion in an accreting 'non-magnetic' white dwarf. *Nature* **552**, 210–213 (2017). doi:10.1038/nature24653 Medline

5. P. F. Wyper, S. K. Antiochos, C. R. DeVore, A universal model for solar eruptions. *Nature* **544**, 452–455 (2017). doi:10.1038/nature22050 Medline

6. H. Carmichael, "A Process for Flares," in *The Physics of Solar Flares, Proceedings of the AAS-NASA Symposium held 28-30 October, 1963 at the Goddard Space Flight Center, Greenbelt, MD*, W. N. Hess, Ed. (National Aeronautics and Space Administration, 1964), vol. 50, p. 451.

7. P. A. Sturrock, Model of the High-Energy Phase of Solar Flares. *Nature* **211**, 695–697 (1966). doi:10.1038/211695a0

8. T. Hirayama, Theoretical model of flares and prominences. *Sol. Phys.* **34**, 323–338 (1974). doi:10.1007/BF00153671

9. R. A. Kopp, G. W. Pneuman, Magnetic reconnection in the corona and the loop prominence phenomenon. *Sol. Phys.* **50**, 85 (1976). doi:10.1007/BF00206193

10. E. Priest, T. Forbes, *Magnetic Reconnection* (Cambridge Univ. Press, 2007).

11. X. Sun, J. T. Hoeksema, Y. Liu, T. Wiegelmann, K. Hayashi, Q. Chen, J. Thalmann, Evolution of magnetic field and energy in a major eruptive active region based on *SDO*/HMI observation. *Astrophys. J.* **748**, 77 (2012). doi:10.1088/0004-637X/748/2/77

12. M. L. DeRosa, C. J. Schrijver, G. Barnes, K. D. Leka, B. W. Lites, M. J. Aschwanden, T. Amari, A. Canou, J. M. McTiernan, S. Régnier, J. K. Thalmann, G. Valori, M. S. Wheatland, T. Wiegelmann, M. C. M. Cheung, P. A. Conlon, M. Fuhrmann, B. Inhester, T. Tadesse, A critical assessment of nonlinear force-free field modeling of the solar corona for active region 10953. *Astrophys. J.* **696**, 1780–1791 (2009). doi:10.1088/0004-637X/696/2/1780

13. Materials and methods are available as supplementary materials.

14. Y. Li, J. C. Xue, M. D. Ding, X. Cheng, Y. Su, L. Feng, J. Hong, H. Li, W. Q. Gan, Spectroscopic Observations of a Current Sheet in a Solar Flare. *Astrophys. J.* **853**, L15 (2018). doi:10.3847/2041-8213/aaa6c0

15. H. P. Warren, D. H. Brooks, I. Ugarte-Urra, J. W. Reep, N. A. Crump, G. A. Doschek, Spectroscopic Observations of Current Sheet Formation and Evolution. *Astrophys. J.* **854**, 122 (2018). doi:10.3847/1538-4357/aaa9b8

16. D. E. Gary, B. Chen, B. R. Dennis, G. D. Fleishman, G. J. Hurford, S. Krucker, J. M. McTiernan, G. M. Nita, A. Y. Shih, S. M. White, S. Yu, Microwave and Hard X-Ray Observations of the 2017 September 10 Solar Limb Flare. *Astrophys. J.* **863**, 83 (2018). doi:10.3847/1538-4357/aad0ef

17. N. Omodei, M. Pesce-Rollins, F. Longo, A. Allafort, S. Krucker, *Fermi* -LAT Observations of the 2017 September 10 Solar Flare. *Astrophys. J.* **865**, L7 (2018). doi:10.3847/2041-8213/aae077

18. D. M. Long, L. K. Harra, S. A. Matthews, H. P. Warren, K.-S. Lee, G. A. Doschek, H. Hara, J. M. Jenkins, Plasma Evolution within an Erupting Coronal Cavity. *Astrophys. J.* **855**, 74 (2018). doi:10.3847/1538-4357/aaad68

19. G. A. Doschek, H. P. Warren, L. K. Harra, J. L. Culhane, T. Watanabe, H. Hara, Photospheric and Coronal Abundances in an X8.3 Class Limb Flare. *Astrophys. J.* **853**, 178 (2018). doi:10.3847/1538-4357/aaa4f5

20. D. Longcope, J. Unverferth, C. Klein, M. McCarthy, E. Priest, Evidence for Downflows in the Narrow Plasma Sheet of 2017 September 10 and Their Significance for Flare Reconnection. *Astrophys. J.* **868**, 148 (2018). doi:10.3847/1538-4357/aaeac4

21. G. M. Nita, J. Hickish, D. MacMahon, D. E. Gary, EOVSA Implementation of a Spectral Kurtosis Correlator for Transient Detection and Classification. *J. Astron. Instrum.* **05**, 1641009 (2016). doi:10.1142/S2251171716410099

22. S. A. Anfinogentov, A. G. Stupishin, I. I. Mysh'yakov, G. D. Fleishman, Record-breaking Coronal Magnetic Field in Solar Active Region 12673. *Astrophys. J.* **880**, L29 (2019). doi:10.3847/2041-8213/ab3042

23. H. Dreicer, Electron and Ion Runaway in a Fully Ionized Gas. I. *Phys. Rev.* **115**, 238–249 (1959). doi:10.1103/PhysRev.115.238

24. J. Qiu, D. E. Gary, G. D. Fleishman, Evaluating Mean Magnetic Field in Flare Loops. *Sol. Phys.* **255**, 107–118 (2009). doi:10.1007/s11207-009-9316-y

25. G. D. Fleishman, V. D. Pal'shin, N. Meshalkina, A. L. Lysenko, L. K. Kashapova, A. T. Altyntsev, A cold flare with delayed heating. *Astrophys. J.* **822**, 71 (2016). doi:10.3847/0004-637X/822/2/71

26. G. D. Fleishman, I. N. Toptygin, *Cosmic Electrodynamics: Electrodynamics and Magnetic Hydrodynamics of Cosmic Plasmas* (Springer 2013).

27. J. T. Dahlin, J. F. Drake, M. Swisdak, The role of three-dimensional transport in driving enhanced electron acceleration during magnetic reconnection. *Phys. Plasmas* **24**, 092110 (2017). doi:10.1063/1.4986211

28. G. D. Fleishman, G. M. Nita, D. E. Gary, Dynamic magnetography of solar flaring loops. *Astrophys. J.* **698**, L183–L187 (2009). doi:10.1088/0004-637X/698/2/L183

29. D. E. Gary, G. D. Fleishman, G. M. Nita, Magnetography of Solar Flaring Loops with Microwave Imaging Spectropolarimetry. *Sol. Phys.* **288**, 549–565 (2013). doi:10.1007/s11207-013-0299-3

30. J. A. Högbom, Aperture Synthesis with a Non-Regular Distribution of Interferometer Baselines. *Astron. Astrophys. Suppl.* **15**, 417–426 (1974).

31. G. A. Dulk, Radio Emission from the Sun and Stars. *Annu. Rev. Astron. Astrophys.* **23**, 169–224 (1985). doi:10.1146/annurev.aa.23.090185.001125

32. G. D. Fleishman, A. A. Kuznetsov, Fast gyrosynchrotron codes. *Astrophys. J.* **721**, 1127–1141 (2010). doi:10.1088/0004-637X/721/2/1127

33. J. A. Nelder, R. Mead, A Simplex Method for Function Minimization. *Comput. J.* **7**, 308–313 (1965). doi:10.1093/comjnl/7.4.308